Orbital flow around a circular cylinder. Part 2. Attached flow at larger amplitudes

By JOHN R. CHAPLIN

Ocean Engineering Research Centre, Department of Civil Engineering, City University, London EC1V 0HB, UK

A time-stepping numerical model of uniform circular orbital flow around a cylinder provides results which are compared with the steady-state predictions of a boundary-layer solution by Riley. At small amplitudes of motion excellent agreement is found in most respects, but in the numerical model the outer recirculating flow and related components of loading do not reach a steady state after any finite time. At a Stokes parameter β of 500, the boundary-layer approach remains reasonably accurate for amplitudes of motion up to about 8% of the cylinder diameter; for amplitudes up to twice this at the same value of β the flow remains largely attached. The strength of the outer recirculating flow is enhanced by nonlinear interactions, but the computed nonlinear loading exceeds that observed in experiments. Flow visualization shows a three-dimensional structure in the flow, and it is argued that this has an important effect on the loading that cannot yet be predicted. A computed force component at a frequency of about 30% of that of the ambient flow is related to the retrogressive motion of vortex structures around the cylinder.

1. Introduction

This paper is concerned with the flow around a cylinder which is driven (without rotation) around a circular path, normal to its axis, in fluid initially at rest. The flow is related to that around a stationary horizontal cylinder beneath waves, aligned so that its axis is parallel with the wave crests. It is indeed the limiting case for waves in deep water, when the cylinder diameter is small in comparison both to its submergence and to the wavelength. In the past, orbital flow around a cylinder has received much less attention than the rectilinear oscillatory case, where it is found that providing that the motion remains attached, potential flow remains a good basis for force predictions. In orbital motion on the other hand, secondary flows generate substantial contributions to the loading even at very small amplitudes (Chaplin 1984*b*; Stansby & Smith 1991).

With the aim of developing a better detailed understanding of attached orbital flow, a numerical solution is described below for the case where the flow is not dominated by the effects of separation. Applications include horizontal pontoons of semi-submersibles and tension leg platforms (Otsuka, Ikeda & Tanaka 1990; Chaplin & Retzler 1991), and the 'Bristol cylinder' wave energy device (Evans 1976); in these cases predictions of loading and response traditionally neglect viscosity.

A steady-state solution for the most important components of the flow around a circular cylinder executing circular orbital motion was obtained by Riley (1971). Longuet-Higgins (1970) had previously shown that steady streaming induces a uniform circulation around the cylinder, with the same sense of motion as that of the

ambient flow. For the non-uniform case of a horizontal cylinder beneath waves, measurements of particle drift velocities at the outer limit of the boundary layer were subsequently found to be compatible with the predicted steady streaming (Chaplin 1984a), but measured forces did not agree well with the implications of a uniform circulation of corresponding strength (Chaplin 1984b). Application of the Kutta–Joukowski theorem, extended to unsteady flow (see Chaplin 1992), suggests that the effect of the induced circulation would be a cancellation of part of the inertia force, so that the effective inertia coefficient C_m would depart from the potential flow value of 2, in accordance with

$$C_m = 2 - 6K_c^2/\pi^2, \tag{1.1}$$

where K_c is the Keulegan–Carpenter number. Though substantial reductions in C_m have been found in experiments in waves at low Keulegan–Carpenter numbers (Chaplin 1984b; Otsuka *et al.*, 1990) the results are generally not in quantitative agreement with (1.1); in most cases the observed reduction in C_m is weaker than that indicated above: in some cases at small submergences it is stronger.

In an attempt to understand the importance of the non-uniformities of wave-induced orbital flow on the circulation, this case was studied with a boundary-layer approach by Chaplin (1992). Though it was found that the relative submergence of the cylinder and the diameter-to-wavelength ratio had significant effects on the strength of the induced circulation, the changes were not sufficient fully to account for the experimental observations.

The boundary-layer solution by Riley (1971) does not extend to a sufficiently high order to provide a direct prediction of non-linear loading due to secondary flow. In any case, for larger amplitudes of motion (or wave heights), but before separation occurs, the solution will become less accurate, as neglected higher-order terms become more important. A third limitation on the application of the boundary-layer solution arises from the fact that it refers to the final steady state, and therefore may not be appropriate physically at any finite time. In the steady-state solution there is uniform circulation around the cylinder, whereas Stansby & Smith (1991) have pointed out that at any finite time the circulation must tend to zero at large distances from the cylinder. Stansby & Smith modelled the flow using the random-vortex method and, in qualitative agreement with experiments, found a substantial reduction in C_m with increasing K_c. The purpose of the work described in the present paper is to explore in more detail the limits of validity of boundary-layer solutions, and to study the way in which the outer recirculating flow (and any associated loading) grows with time.

The flow was computed with a Navier–Stokes time-stepping code which is described in §2. Sections 3 and 4 present the results which, where appropriate, are in excellent agreement with Riley's boundary-layer solution. In some respects however they reveal differences that can be attributed to the truncation of Riley's series expansions. At larger amplitudes of motion, with the flow still attached, other nonlinearities become apparent. The secondary flow is enhanced, and as the Keulegan–Carpenter number approaches 1.5, the viscosity-induced loading negates almost one-half of the potential flow force for the case of a stationary cylinder. Comparisons with available experimental results are discussed in §5, which introduces also some new flow visualization, showing for the first time a three-dimensional structure in the flow around a horizontal cylinder beneath waves.
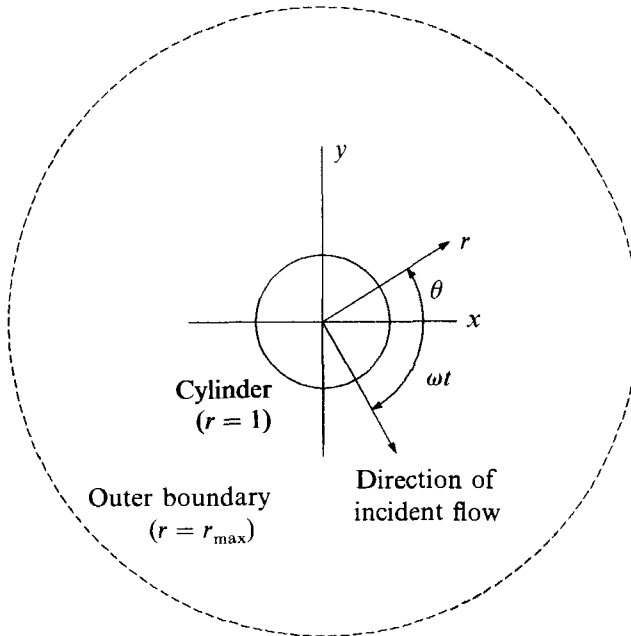
FIGURE 1. Definition sketch for the numerical model.

2. The Navier–Stokes code

The solution is obtained for the region shown in figure 1, and is developed in terms of the stream function and vorticity, whose variations in the tangential direction at each time step are expressed at each discrete radius as a Fourier series of spatial frequency components. This approach (a generalization of that used by Patel 1976) was chosen for the present problem since for the more general case of a horizontal cylinder beneath waves, the conditions at the outer boundary may be readily expressed in terms of their spatial frequency components. Also, the computed results are obtained in a form in which they may be compared directly with individual terms in Riley's solution of the boundary-layer problem.

The reference frame is fixed on the cylinder; for the particular case of uniform circular orbital flow, some economies could be obtained by using a frame which is rotating with the direction of the ambient flow. We choose however the more general case, since the purpose of subsequent computations was to study non-uniform flows, which do not offer the same symmetry.

Taking as reference length the cylinder radius c, as reference velocity the magnitude of the particle velocity U at the cylinder location in the undisturbed flow, the vorticity transport equation may be expressed for polar co-ordinates fixed on the cylinder as

$$\frac{\partial \zeta}{\partial t} + \frac{1}{r}\left(\frac{\partial \psi}{\partial \theta}\frac{\partial \zeta}{\partial r} - \frac{\partial \psi}{\partial r}\frac{\partial \zeta}{\partial \theta}\right) = \frac{2}{Re}\nabla^2\zeta. \tag{2.1}$$

The stream function is related to the radial and tangential velocity components by

$$v_r = \frac{1}{r}\frac{\partial \psi}{\partial \theta}, \quad v_\theta = -\frac{\partial \psi}{\partial r}. \tag{2.2}$$

The vorticity (measured positive anticlockwise) satisfies

$$\zeta = -\nabla^2\psi, \tag{2.3}$$

and Re is the Reynolds number $2Uc/\nu$. The amplitude of the motion is expressed in terms of the Keulegan–Carpenter number $K_c = UT/2c$, where T is the period, and $\beta = Re/K_c$.

The stream function and vorticity are expanded in terms of spatial frequency components:

$$\psi(\xi, \theta, t) = \sum_{n=0}^{N} f_n(\xi, t) \cos n\theta + g_n(\xi, t) \sin n\theta, \tag{2.4}$$

$$\zeta(\xi, \theta, t) = -\sum_{n=0}^{N} F_n(\xi, t) \cos n\theta + G_n(\xi, t) \sin n\theta, \tag{2.5}$$

where $\xi = \ln r$. Equation (2.3) implies

$$F_n = e^{-2\xi}\left(\frac{\partial^2 f_n}{\partial \xi^2} - n^2 f_n\right), \quad G_n = e^{-2\xi}\left(\frac{\partial^2 g_n}{\partial \xi^2} - n^2 g_n\right), \quad n = 0, 1, \dots, N. \tag{2.6}$$

Substituting (2.4) and (2.5) into (2.1), and separating the frequency components leads to

$$e^{2\xi}\dot{F}_0 = \frac{2}{Re}\frac{\partial^2 F_0}{\partial \xi^2} + \frac{1}{2}\sum_{m=1}^{N} m\left(\frac{\partial G_m}{\partial \xi}f_m - \frac{\partial F_m}{\partial \xi}g_m + \frac{\partial f_m}{\partial \xi}G_m - \frac{\partial g_m}{\partial \xi}F_m\right), \tag{2.7}$$

$$G_0 = 0, \tag{2.8}$$

$$e^{2\xi}\dot{F}_n = \frac{2}{Re}\left(\frac{\partial^2 F_n}{\partial \xi^2} - n^2 F_n\right) + \frac{n}{2}\left(-\frac{\partial F_0}{\partial \xi}g_n + \frac{\partial f_0}{\partial \xi}G_n\right)$$
$$+ \frac{1}{2}\sum_{m=1}^{N} m\left[\left(\frac{\partial G_{m-n}}{\partial \xi} + \frac{\partial G_{m+n}}{\partial \xi}\right)f_m - \left(\frac{\partial F_{m-n}}{\partial \xi} + \frac{\partial F_{m+n}}{\partial \xi}\right)g_m\right.$$
$$\left. + \left(\frac{\partial f_{m-n}}{\partial \xi} + \frac{\partial f_{m+n}}{\partial \xi}\right)G_m - \left(\frac{\partial g_{m-n}}{\partial \xi} + \frac{\partial g_{m+n}}{\partial \xi}\right)F_m\right], \quad n = 1, 2, \dots, N, \tag{2.9}$$

$$e^{2\xi}\dot{G}_n = \frac{2}{Re}\left(\frac{\partial^2 G_n}{\partial \xi^2} - n^2 G_n\right) + \frac{n}{2}\left(\frac{\partial F_0}{\partial \xi}f_n - \frac{\partial f_0}{\partial \xi}F_n\right)$$
$$+ \frac{1}{2}\sum_{m=1}^{N} m\left[\left(\frac{\partial F_{m-n}}{\partial \xi} - \frac{\partial F_{m+n}}{\partial \xi}\right)f_m + \left(\frac{\partial G_{m-n}}{\partial \xi} - \frac{\partial G_{m+n}}{\partial \xi}\right)g_m\right.$$
$$\left. - \left(\frac{\partial f_{m-n}}{\partial \xi} - \frac{\partial f_{m+n}}{\partial \xi}\right)F_m - \left(\frac{\partial g_{m-n}}{\partial \xi} - \frac{\partial g_{m+n}}{\partial \xi}\right)G_m\right], \quad n = 1, 2, \dots, N, \tag{2.10}$$

where $\dot{F}$ denotes $\partial F/\partial t$, etc. Equations (2.6)–(2.10) represent the core of the numerical method. The variables $F_0, F_1 \dots F_N$, $G_1, G_2 \dots G_N$, $f_0, f_1 \dots f_N$, $g_1, g_2 \dots g_N$, are functions only of ξ and t, and are discretized at points corresponding to constant increments $\Delta\xi$, i.e. exponentially increasing increments in r. The solution advances through time increments Δt, at each step updating F and G with finite-difference approximations to (2.7)–(2.10) using central differences in a fully implicit iterative scheme. The updated f and g are found from (2.6), each of which reduces to a tridiagonal system at each frequency.

The boundary conditions on the cylinder $\xi = 0$, are $f_n = g_n = 0$, for all n, and a Woods condition for the vorticity,

$$\zeta_w = -\frac{6\psi_1 + \Delta\xi^2\zeta_1}{2(\Delta\xi^2 + \Delta\xi^3)} \tag{2.11}$$

(where subscripts w and 1 refer to a point on the wall and a point one cell away), applied at all frequencies.

On the outer boundary $\xi = I\Delta\xi$, the vorticity at all frequencies, and the stream function at frequencies $n = 2, 3, ..., N$, are put equal to zero. At frequency $n = 1$, the stream function on the outer boundary is made to match the tangential flow corresponding to the undisturbed orbital motion:

$$f_1(I\Delta\xi, t) = \cos(\pi t/K_c), \quad g_1(I\Delta\xi, t) = \sin(\pi t/K_c). \tag{2.12}$$

Equations (2.12) imply a clockwise orbital flow, resembling the case of a wave train passing from left to right.

A potential advantage of this spectral method for the present problem is that the oscillatory flow can be used to drive the solution from the outer boundary of the computational domain, while a separate boundary condition is available there for the zero-frequency flow f_0. This component of the flow originates from within the boundary layer on the cylinder, and must be allowed to spread outwards without unnatural disturbance. However, in all computations the magnitude of the zero-frequency flow near the outer boundary was extremely small at all times, and the outer boundary condition adopted was simply $\partial f_0/\partial \xi = 0$, representing the requirement that the circulation tend to zero at all finite times at large distances from the cylinder (Wu 1981; Stansby & Smith 1991). Tests were carried out to confirm that the outer boundary was in fact far enough away to avoid any significant effects on the computed flow.

Forces and moments on the cylinder may be computed from the surface vorticity and its radial gradient. On the cylinder surface, the pressure and shear stress are given by

$$\frac{\partial p}{\partial \theta} = \frac{4}{Re}\frac{\partial \zeta}{\partial r}, \quad \sigma = \frac{4}{Re}\zeta \quad \text{on} \quad r = 1, \tag{2.13}$$

where the reference stress is taken as $\frac{1}{2}\rho U^2$. The components of force and moment experienced by the cylinder are

$$F_{xp} = -\frac{4\pi}{Re}G_1', \quad F_{yp} = \frac{4\pi}{Re}F_1', \tag{2.14}$$

$$F_{xs} = \frac{4\pi}{Re}G_1, \quad F_{ys} = -\frac{4\pi}{Re}F_1, \tag{2.15}$$

$$M = -\frac{8\pi}{Re}F_0, \tag{2.16}$$

all evaluated at $r = 1$; $F_1' = \partial F_1/\partial r$, etc. Subscripts p and s refer to components due to pressure and shear stress respectively, and M is the moment, measured anticlockwise. Computed forces due to pressure are presented below after subtraction of the potential flow force $4\pi^2/K_c$.

For each condition that was computed, checks were carried out to ensure that the radius of the computational domain r_{max}, the number of frequency components, and the discretization intervals did not significantly affect the most sensitive result of interest, namely the part of the pressure-induced force that is due to viscosity. At small K_c values this is a very small proportion of the total force, and (because it is derived from the gradient of vorticity on the cylinder surface) it is also very sensitive

K_c	β	$r_{\max}$	N
0.1	10	300	5
0.5	500	8	9
1.0	500	16	13
1.5	500	16	30
0.1	1000	7	5

TABLE 1. Radius of the computational domain, and number of frequencies for representative cases.

to discretization errors. In all cases, the time step Δt was less than 1/800th of the period of the oscillation, and

$$\Delta \xi < 2 \, (2 \, \Delta t/Re)^{\frac{1}{2}}. \tag{2.17}$$

Computational parameters for representative cases are given in table 1. The number of spatial frequency components N was always sufficient to ensure that the magnitude of the smallest component was less than 0.1 % of that of the largest. Run-times on a Sun Sparcstation were about $I \times N^2 \times 10^{-4}$ s per time step. For each case, the amplitude of the motion was ramped up linearly over one period.

3. Results for small K_c

3.1. Riley's solution

At small Keulegan–Carpenter numbers and high values of β, one may expect computed results to agree well with the boundary-layer solution in all respects except those associated with transient processes. Some comparisons are described below, but first we point out the relevant features of Riley's boundary-layer solution.

The solution is obtained in terms of matched asymptotic expansions for the stream function in the inner (boundary layer) and outer (predominantly irrotational) regions. We summarize Riley's results here and in the Appendix in terms of the various components of the tangential velocity, and the viscosity-induced forces. For the inner region, the tangential velocity may be written

$$V_\theta = U_0 + \sum_{n=1} U_n \cos n\phi + V_n \sin n\phi, \tag{3.1}$$

with a similar series for the outer region,

$$v_\theta = u_0 + \sum_{n=1} u_n \cos n\phi + v_n \sin n\phi, \tag{3.2}$$

where $\phi = \theta + \omega t$ (see figure 1). The velocity components U_n, etc. are normalized with reference to U; they represent parts of Riley's double series for the complete flow, and are set out in the Appendix in terms of the parameters β and K_c. The radial ordinate for the inner region is

$$\eta = \frac{1}{2}(r-1)(\pi\beta)^{\frac{1}{2}}. \tag{3.3}$$

The outer flow u_0 represents the potential vortex of circulation

$$\Gamma_0 = 6K_c \tag{3.4}$$

identified by Longuet-Higgins (1970), and is of particular interest here in view of its connection with nonlinear loading.

The loading due to viscosity on the cylinder may be separated into force components that are either in phase with the velocity or in phase with the acceleration; in each case the force is due partly to pressure and partly to shear stress. The four force components are accordingly denoted F_{vp}, F_{vs}, F_{ap} and F_{as}. There is also a moment M.

Steady-state forces may be derived from Riley's solution for the stream function in the inner region. On this basis

$$F_{vp} = \frac{4\pi^2}{K_c}\left\{\left(\frac{1}{\pi\beta}\right)^{\frac{1}{2}} - \frac{1}{\pi\beta}\right\} + O(\beta^{-\frac{3}{2}}) + O(K_c), \tag{3.5}$$

$$F_{ap} = F_{as} = \frac{4\pi^2}{K_c}\left(\frac{1}{\pi\beta}\right)^{\frac{1}{2}} + O(\beta^{-\frac{3}{2}}) + O(K_c), \tag{3.6}$$

$$F_{vs} = \frac{4\pi^2}{K_c}\left\{\left(\frac{1}{\pi\beta}\right)^{\frac{1}{2}} + \frac{1}{\pi\beta}\right\} + O(\beta^{-\frac{3}{2}}) + O(K_c), \tag{3.7}$$

and the moment is given by

$$M = -8\pi\left(\frac{1}{\pi\beta}\right)^{\frac{1}{2}} + O(\beta^{-\frac{3}{2}}) + O(K_c). \tag{3.8}$$

Though an outer circulation is present (associated with u_0), its effect does not appear in (3.5)–(3.8) since the inner expansion was not extended to the term $O(K_c^2)$ (originally $O(\epsilon^2)$ in equation (19) of Riley 1971). This is the term through which the effect of the circulation on the loading would be first expected. Were the consequences of the circulation to be included, it would be reasonable to look for a reduction in F_{ap}, due to a process similar to the Magnus effect.

3.2. *Computed results*

In the numerical solution, there is no distinction between the inner and outer regions. But for clarity, the two parts of the analytical solution are compared separately with the numerical results in figure 2. In each region, each component of the first three spatial frequency components is compared, at $K_c = 0.1$ and at $\beta = 10$, 100, and 1000. (At $K_c = 0.1$, the amplitude of the motion is about 1.6 % of the cylinder diameter.)

In studying these comparisons, it must be remembered that the boundary-layer solution refers to the steady state at infinite time. At frequencies 1 and 2, on figure 2 (*c–j*) are superimposed numerical results (for $\beta = 10$ and 1000) at times corresponding to four and 60 cycles of oscillation. Very little change occurs in these components over this interval, suggesting that the numerical results are in these respects very close indeed to a steady state. On the other hand, the zero-frequency component undergoes continuous change, as discussed below.

At frequencies 1 and 2, all numerical results shown in figure 2 converge as expected towards the analytical solution as the value of β is increased. But particularly close to the boundary and at frequency 2 there are still significant differences at $\beta = 1000$ arising from absent $O(\beta^{-\frac{1}{2}})$ terms in the boundary-layer expansion.

Unlike the components at spatial frequencies 1 and 2, the uniform flow u_0 spreads continuously with time, and is evidently in this respect uncoupled from other parts of the motion. Its computed distributions after various times at $\beta = 10$ and 1000 are
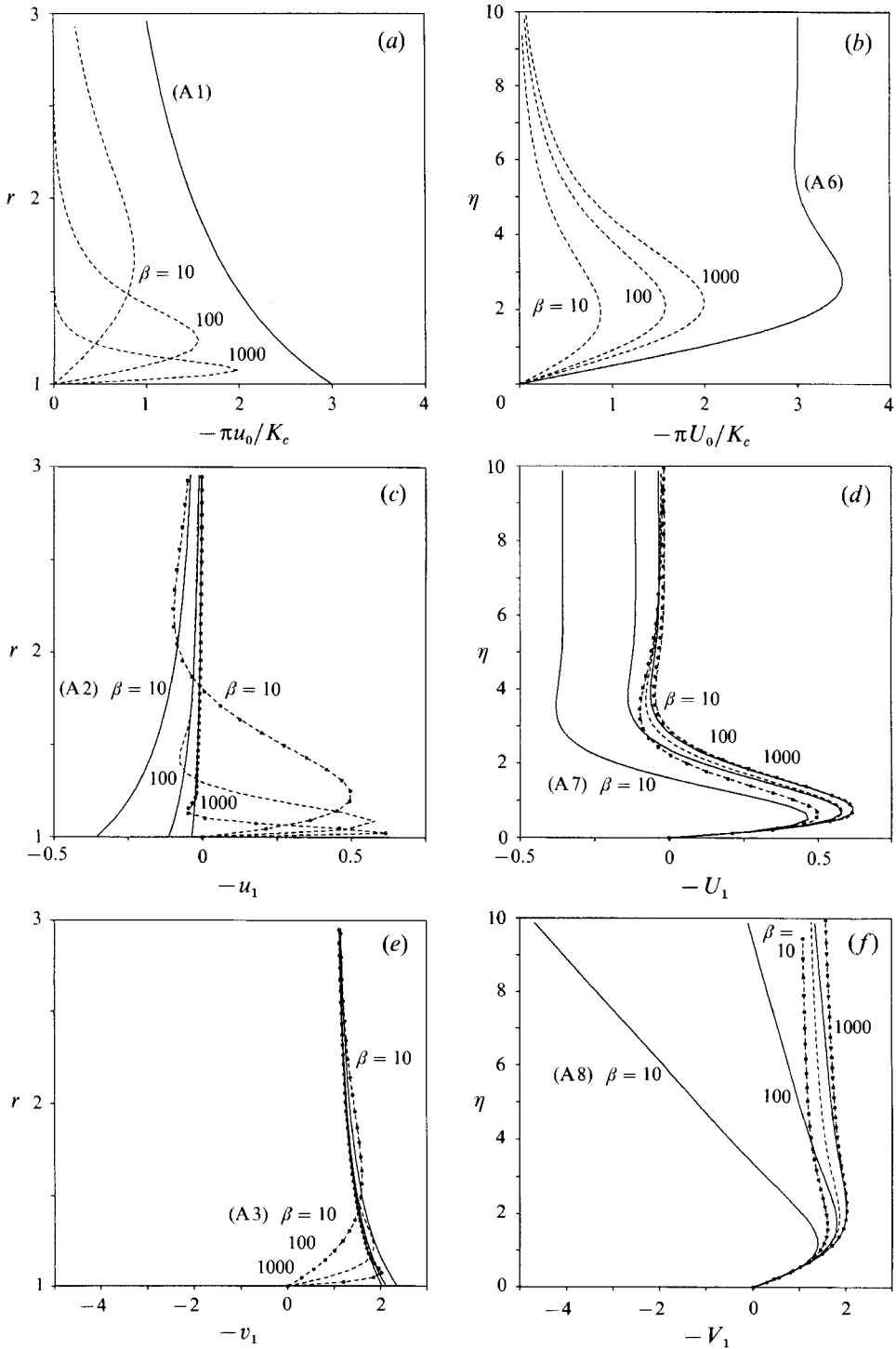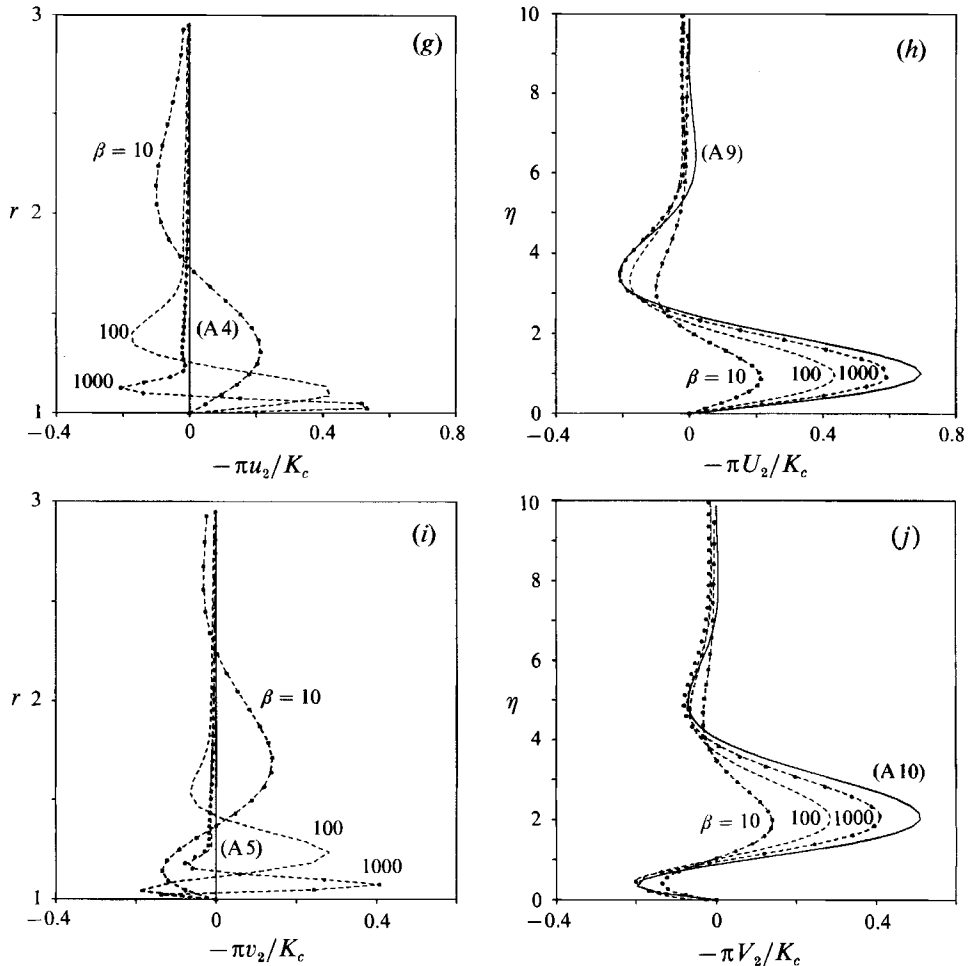
FIGURE 2 (*a–f*). For caption see facing page

FIGURE 2. Tangential velocity components computed after four (-----) and 60 ($\cdot-\cdot-\cdot-\cdot$) cycles at $K_c = 0.1$ compared with predictions from Riley (1971): (a) and (b) show components at spatial frequency $n = 0$; (c) to (f) those at spatial frequency $n = 1$; (g) to (j) those at spatial frequency $n = 2$. In each case the left and right diagrams show respectively the velocity profiles for Riley's outer and inner regions.

plotted in figure 3, and suggest a slow convergence with time towards the distribution given by the boundary-layer solution ((A 1 and A 6)), which in the outer region is a potential vortex.

With reference to the steady-state solution, Riley (1971) noted that in the outer region, the cylinder has the same effect as one rotating on its axis with angular velocity $3K_c/\pi$. The present results allow this analogy to be tested also in the transient state. The flow at time t generated by a cylinder suddenly brought into rotation at $t = 0$ with a surface speed $u_s = 3K_c/\pi$, in infinite fluid otherwise at rest, is given by

$$\frac{v_\theta}{u_s} = \frac{1}{r} + \frac{2}{\pi} \int_0^\infty \frac{\exp\left(-2tx^2/Re\right)}{x} \frac{J_1(xr)\,Y_1(x) - Y_1(xr)\,J_1(x)}{J_1^2(x) + Y_1^2(x)}\,\mathrm{d}x \qquad (3.9)$$

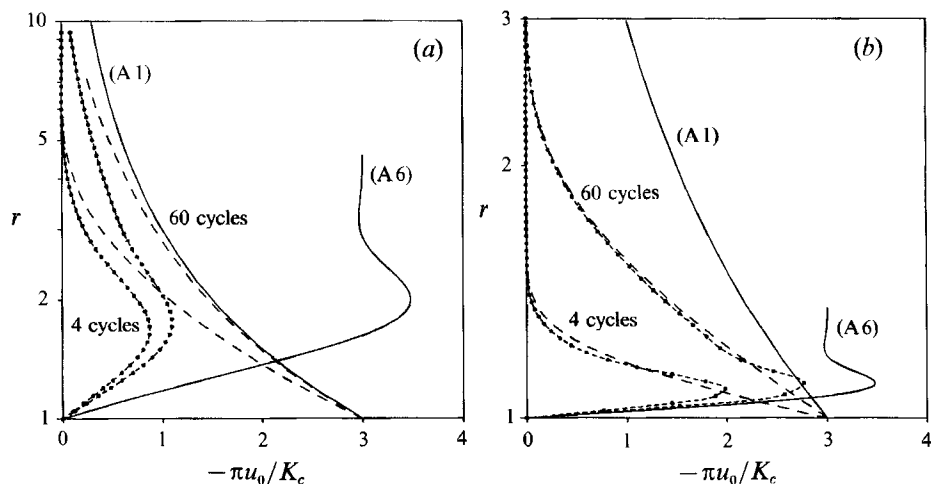(Goldstein 1932), using velocity and length scales as before. J_1 and Y_1 are first-order

FIGURE 3. Velocity components at $K_c = 0.1$, at spatial frequency $n = 0$; and (a) $\beta = 10$, (b) 1000: —·—·—·—·—, orbital flow; — — —, rotating cylinder.

Bessel functions of the first and second kind. Figure 3 includes the velocity distributions (3.9) calculated for the same times as those at which the orbital flow has been computed. Outside the boundary layer, the respective velocity distributions converge as β is increased, suggesting that at finite times, as well as in the steady state, the cylinder generates the same flow at large distances as one rotating with surface speed $3K_c/\pi$.

Computed forces and moments at the end of the fourth cycle at $K_c = 0.01$ and 0.1 are compared in tables $2(a, b)$ with the implications of (3.5)–(3.8). Forces due to shear (F_{vs} and F_{as}) are in very close agreement throughout. At $\beta = 500$ and $K_c = 0.1$ they depart from (3.6) and (3.7) by less than 0.16% (At $\beta = 483$ Stansby & Smith found the corresponding difference to be about 1.7%.) For $K_c = 0.1$ the present results for F_{vp}, F_{ap} and M are plotted in figure 4, showing that F_{vp} also comes very close to the boundary-layer solution at the higher values of β. Like F_{vs} and F_{as}, F_{vp} quickly achieved a steady state; values at the end of the fourth and at the end of the 60th cycle differed by less than 0.17% at $\beta = 10$ and 1000. Computed results for F_{ap} and M on the other hand did not become steady even after 60 cycles, as shown in figure 5 for $\beta = 1000$. Both these components are closely related to the outer recirculating flow.

The moment exerted on the cylinder is equal to the rate of change of the integral, over the whole fluid, of the second moment of vorticity (Wu 1981). Only the recirculating motion f_0 can contribute to this, since all other components integrate to zero. In the transient state the moment is therefore closely linked with the changing distribution of the zero-frequency flow discussed above, and no steady state can be expected after any finite time. In the steady state corresponding to infinite time, the existence of a finite moment (3.8) acting on the cylinder implies a continual increase in the total angular momentum of the fluid. This is not incompatible with the purely periodic nature of the steady-state motion, since the total angular momentum of the fluid would then be infinite anyway. (The related case of a single spinning cylinder is discussed by Batchelor 1967, p. 203.)

The negative drift in F_{ap} shown in figure 5 may also be related to the outwards spread of the recirculating flow, since the growing tangential velocity outside the

(a)

β	F_{vp}		F_{ap}		F_{vs}		F_{as}		M	
	(1)	(2)	(1)	(2)	(1)	(2)	(1)	(2)	(1)	(2)
10	828.9	578.7	688.8	704.3	822.8	830.0	703.9	704.3	1.811	4.484
100	234.5	210.2	219.9	222.7	234.9	235.3	222.7	222.7	0.8411	1.418
1000	67.64	69.18	69.45	70.43	71.58	71.69	70.49	70.43	0.3072	0.4484

(b)

β	F_{vp}		F_{ap}		F_{vs}		F_{as}		M	
	(1)	(2)	(1)	(2)	(1)	(2)	(1)	(2)	(1)	(2)
10	83.12	57.87	68.88	70.43	82.30	83.00	70.43	70.43	1.812	4.484
100	23.50	21.02	21.57	22.27	23.47	23.53	22.22	22.27	0.8411	1.418
500	9.708	9.710	9.342	9.961	10.20	10.21	9.969	9.961	0.4221	0.6341
1000	6.701	6.918	6.484	7.043	7.151	7.169	7.050	7.043	0.3078	0.4484

TABLE 2. Computed force components at the end of the fourth cycle (1), compared with steady-state results (2) from Riley (1971); (a) $K_c = 0.01$, (b) $K_c = 0.1$.
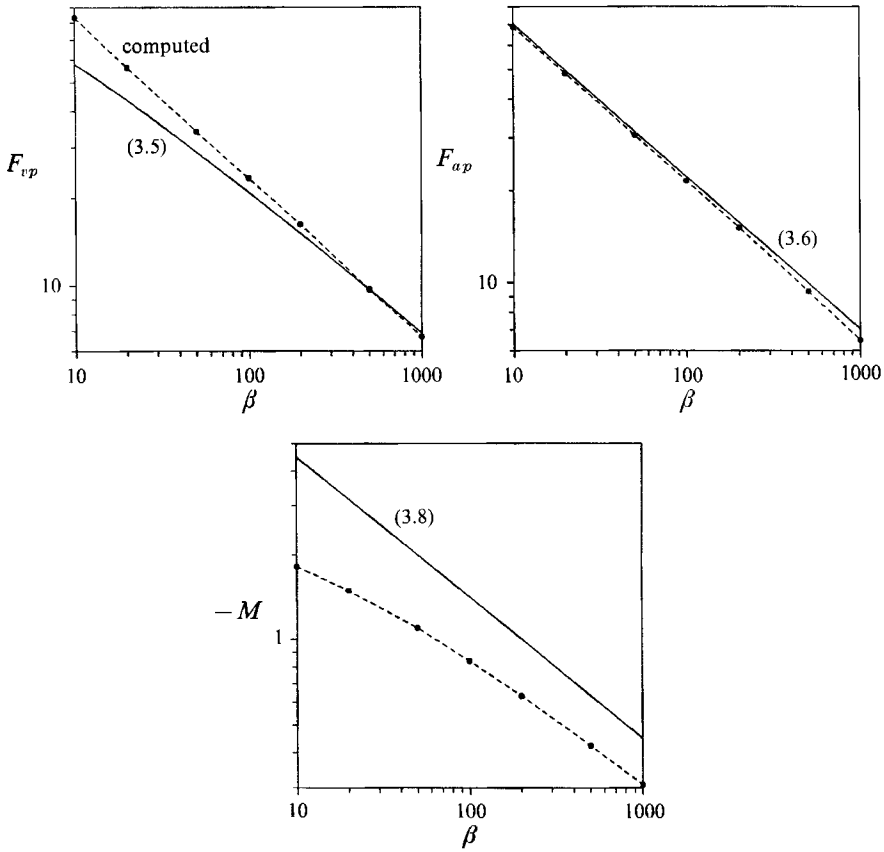
FIGURE 4. Forces due to pressure, and the moment, computed after four cycles at $K_c = 0.1$.
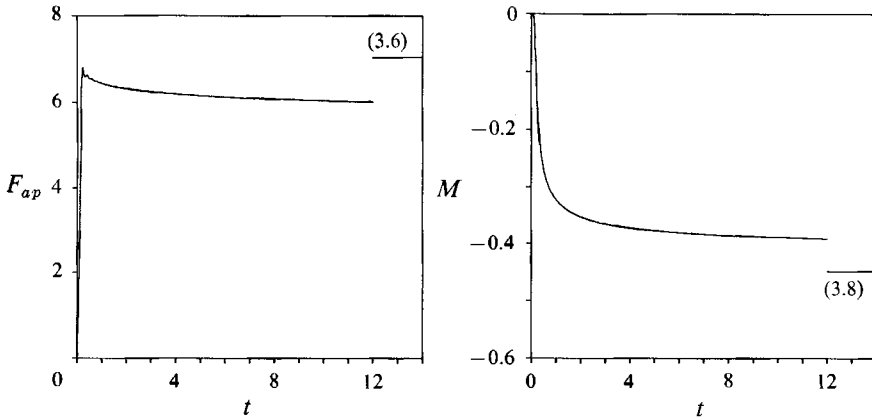

FIGURE 5. Time dependence of F_{ap} and M for $K_c = 0.1$ and $\beta = 1000$.

boundary layer continually enhances the pressure difference across the cylinder in
the direction normal to that of the incident ambient velocity. Formally, the lift is
proportional to the rate of change of the first moment of the vorticity field (Wu
1981). By the Kutta–Joukowski theorem extended to unsteady flow (Chaplin 1992)

the steady-state circulation (3.4) would suggest a contribution $-12K_c$ to F_{ap} (corresponding to the reduction of $6K_c^2/\pi^2$ in C_m given in (1.1)). As expected, no steady state was achieved in the computations, but after 60 cycles, F_{ap} reached 6.017, or $10.26K_c$ less than the value given by (3.6). (It should be noted that (3.4) neglects terms of order $\beta^{-\frac{1}{2}}$ that may be significant at $\beta = 1000$.)

The results presented above have demonstrated the accuracy of the numerical model; in the next section it is applied at higher Keulegan–Carpenter numbers, where nonlinear viscous effects become much more important, and where there is no applicable analytical solution.

4. Results for higher Keulegan–Carpenter numbers

This section is concerned with a range of higher K_c values, for which the flow is nevertheless predominantly attached. We focus on $\beta = 500$, which, as has been shown above, is sufficiently high for many features of the flow to have lost all but their primary dependence on β. It is also in a range for practical purposes of experimentation.

Figure 6 shows the first three spatial frequency components of the tangential flow after eight cycles, for $K_c = 0.5$, 1.0 and 1.5. At $K_c = 0.5$, the flow remains for the most part in reasonable agreement with Riley's solution. Also, the outer recirculating flow again matches that due to a rotating cylinder in initially still fluid (figure 6a). At $K_c = 1.0$ most components of the flow reveal significant changes. At $K_c = 1.5$ major new contributions have appeared, and there is a substantial increase in the thickness of the boundary layer. The outer recirculating flow, evidently enhanced by nonlinear interactions, is now considerably stronger than that corresponding to the rotating cylinder case, suggesting a related growth in nonlinear loading. At $K_c = 1.5$, the maximum value of U_0 in figure 6(a) is about 5% greater than the magnitude of the incident flow. Significant contributions also appear for the first time at higher frequencies, though these are not shown here.

For the higher Keulegan–Carpenter numbers, the force components are plotted against time in figure 7, showing that in most cases they have not reached a steady state. The force components after eight cycles are plotted against K_c in figure 8, which shows that the greatest departures from the boundary-layer solution again occur in F_{ap} and M. These are the components shown above to be most strongly related to the outer recirculating flow. Also plotted in figure 8 is the force represented by (1.1), which corresponds to the steady-state circulation (3.4). This differs from the computed result because the outer flow has a nonlinear component as mentioned above, and because the flow has not approached a steady state. Results derived from Stansby & Smith (1991) using a very different numerical model with an impulsive start are shown to be in good agreement with the present data.

For K_c above 1.3, there was a very rapid increase in the number of frequency components required to satisfy the criteria of §2, and at $K_c = 1.6$ the computational demands of the solution at this degree of precision became impracticable. Slow oscillations first appeared in the force records (figure 7) at $K_c = 1.3$, and became stronger thereafter. They have roughly equal amplitudes in both orthogonal directions, and a frequency about 30% less than that of the ambient motion; the component that appears in F_{ap} leads that in F_{vp} by about 90°. This suggests that the flow is not entirely phase locked to the ambient motion, but has a component that progresses around the cylinder in the opposite direction. A sequence of stream function and vorticity plots is shown in figure 9 for $K_c = 1.5$, at time intervals
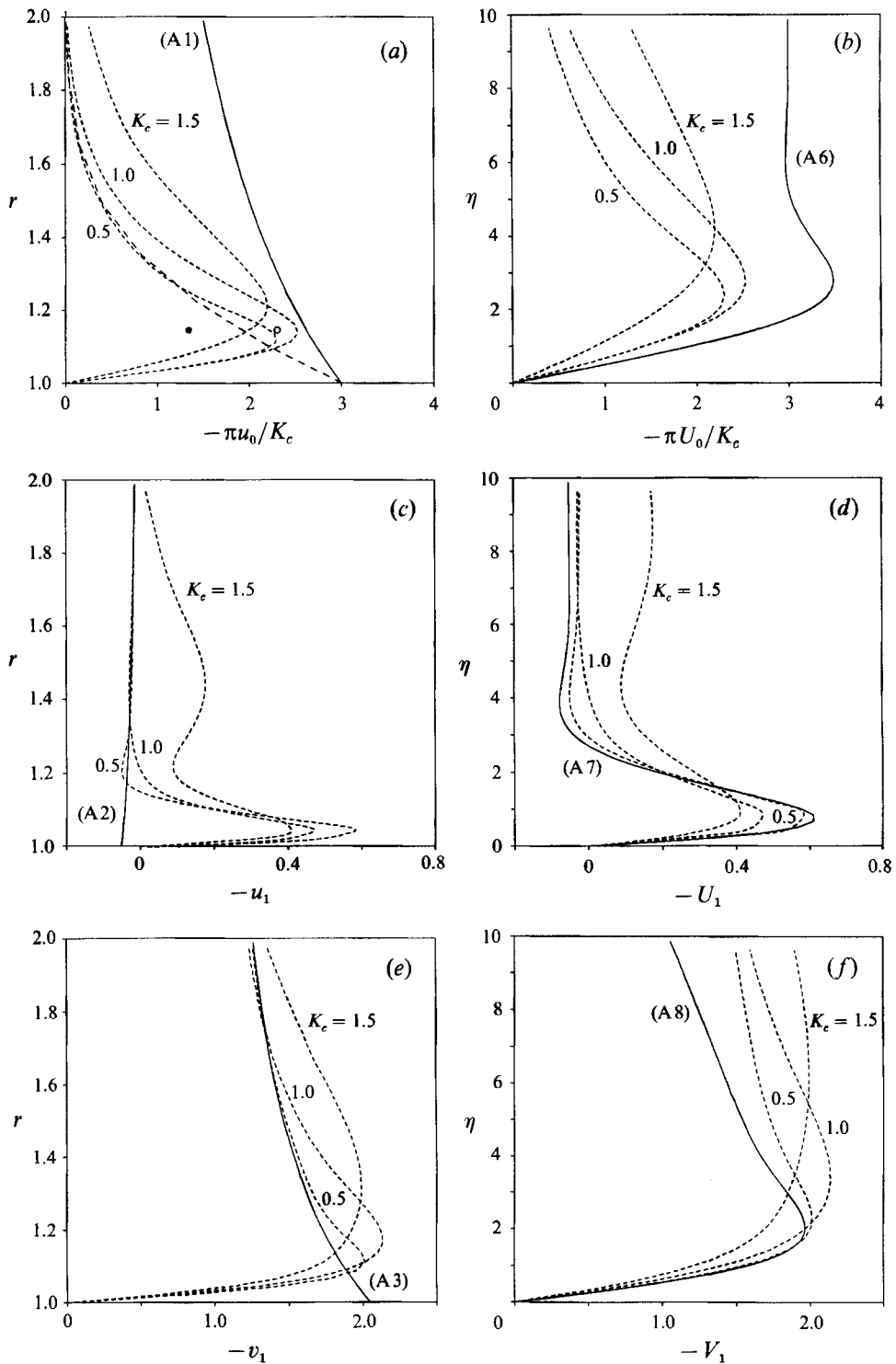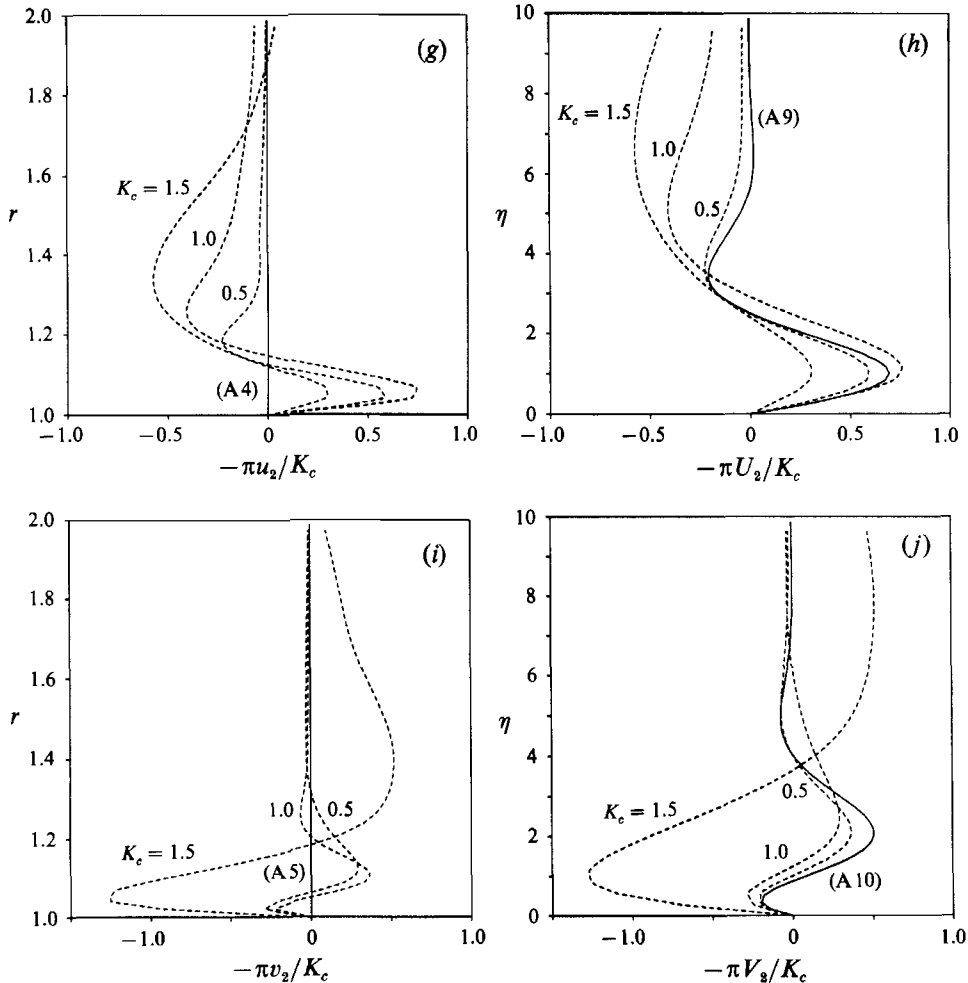
FIGURE 6(a–f). For caption see facing page.

FIGURE 6. Velocity components computed after eight cycles (----) for $\beta = 500$ at $K_c = 0.5$, 1.0 and 1.5, compared with predictions from Riley (1971). The layout of the diagrams is the same as in figure 2. In (a) the long-dashed line shows results for a rotating cylinder, and results of Otsuka *et al.* (1990) at $K_c = 1.0$ (○) and $K_c = 1.5$ (●).

corresponding to one-eighth of the orbital period. The orientation of the diagrams has been altered so that the flow in each case is seen as coming from the left. Also, the radial distance outside the cylinder in the vorticity plots is magnified 5 times. The vorticity structures on the upper side of the cylinder proceed anticlockwise, in the direction opposite to that of the ambient flow. Since the vorticity in this region is predominantly clockwise, the motion can be interpreted as the result of interaction between centres of vorticity and their images in the cylinder surface. As they approach the upstream side of the cylinder, regions of clockwise vorticity become weaker, suggesting cancellation with vorticity of opposite sense of rotation that originates on the other side. This retrogressive motion of vorticity can be associated with the computed non-harmonic component in the loading. In a fixed reference frame, the force component would have a frequency of about 30% of that of the ambient flow. A different process by which vorticity becomes 'wrapped around' the cylinder is described by Stansby & Smith (1991).
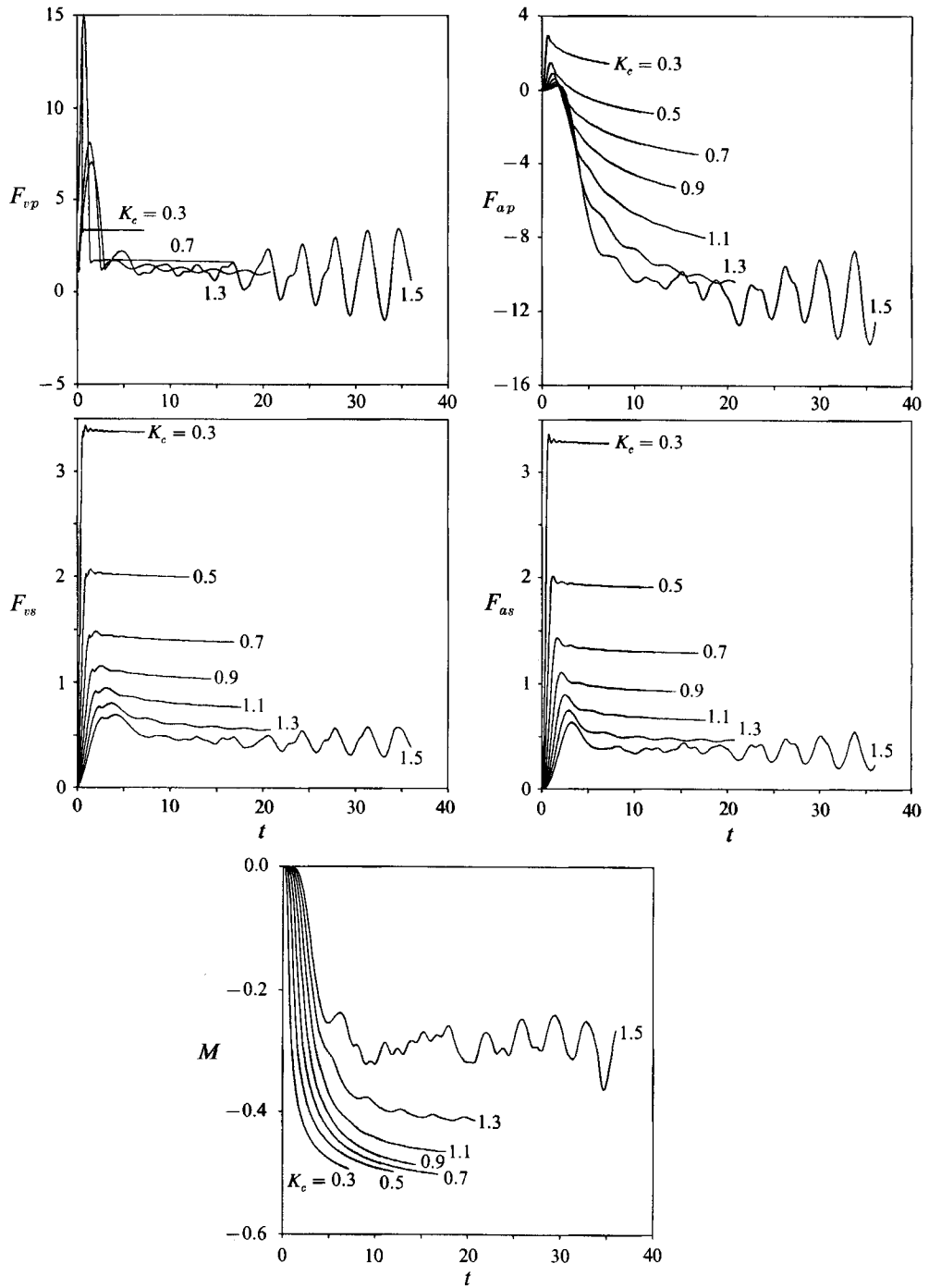
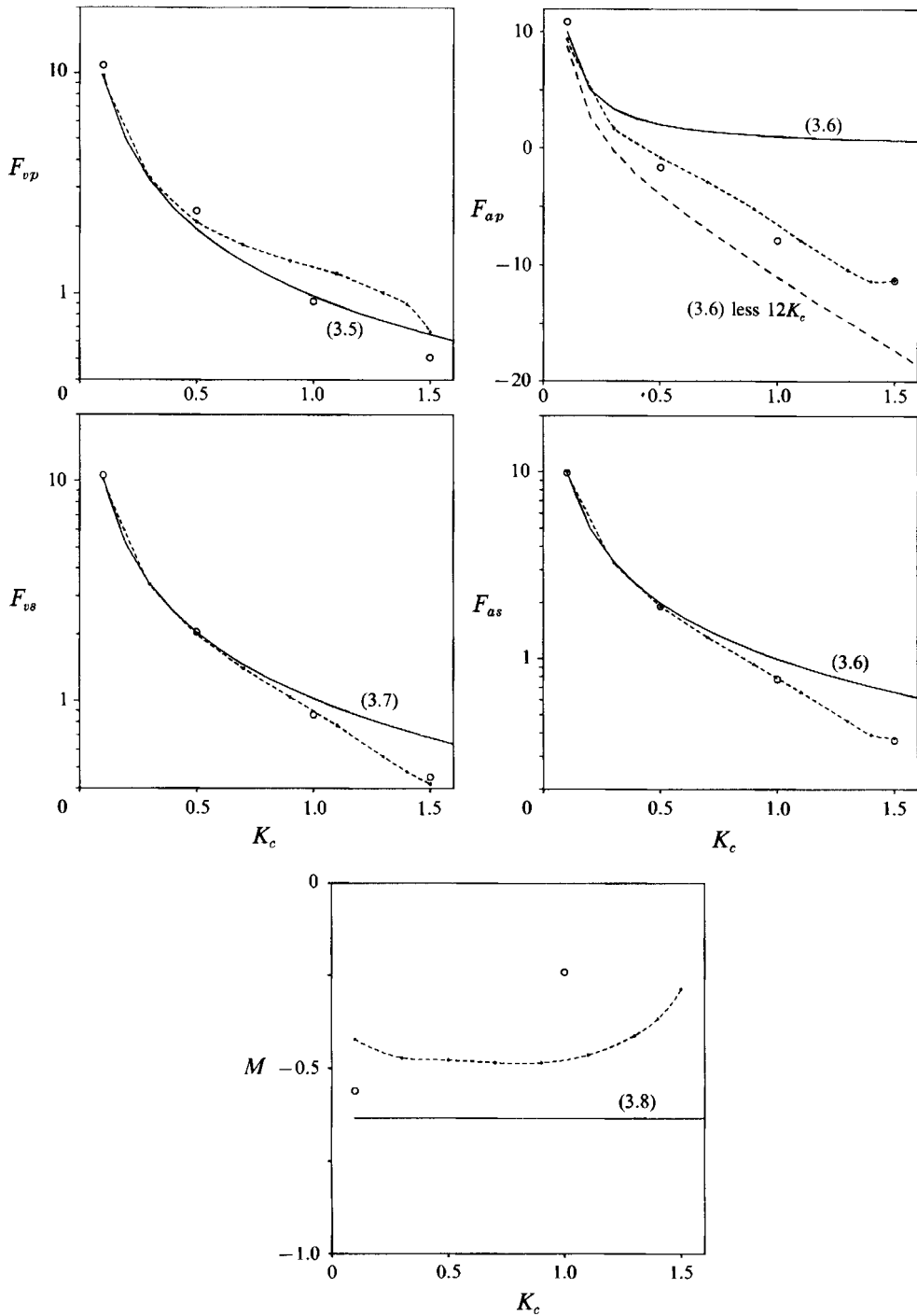FIGURE 7. Time dependence of force components at $\beta = 500$.

FIGURE 8. Force components computed after eight cycles at $\beta = 500$ $(- \cdot - \cdot -)$ compared with Riley (1971) (———) and Stansby & Smith (1991) at times between 11 and 40 cycles $(\circ)$.
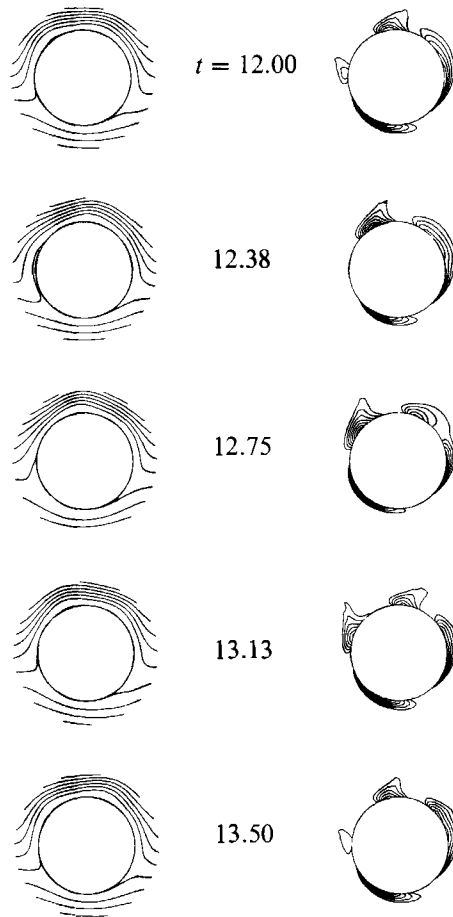
FIGURE 9. Stream function and vorticity contours for $K_c = 1.5$, $\beta = 500$. The orientation of the figures is such that the flow is directed from the left in all cases. In the vorticity plots, the radial distance outside the cylinder is magnified 5 times.

Some computations carried out at $\beta = 5000$ showed the same behaviour, but in this case slow oscillations in the force records first appeared at $K_c = 0.9$.

5. Experimental comparisons

Comparable force measurements have been made on a deeply submerged stationary horizontal cylinder beneath waves by Chaplin (1984b) and Otsuka et al. (1990), and on a cylinder driven around a circular path by Chaplin & Retzler (1991). In the experiments the inertia coefficient approximately followed a relationship of the form of equation (1.1), but with $6/\pi^2$ replaced by a factor of between 0.16 and 0.21. These values indicate a rather weaker nonlinear force than that computed above, which points to a factor of about 0.38. But it should be noted that there were important differences between the numerical and experimental conditions. In the experiments β was in the range 1000 to 10000, and in most cases the flow would have been partly turbulent (on the basis of evidence from Sarpkaya 1986 for rectilinear oscillatory flow). Second, the computations assume that also the mean features of the flow are two-dimensional. Third, the numerical results do not in general refer to a
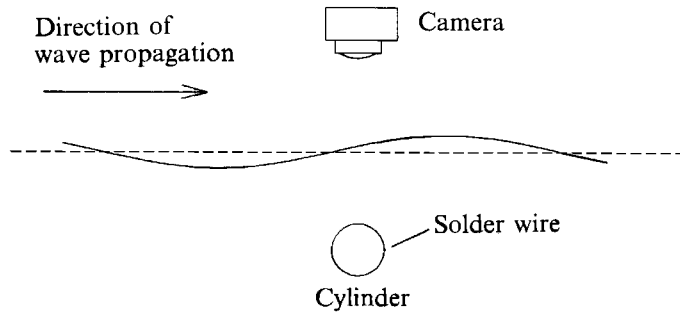
FIGURE 10. General arrangement for the flow visualization experiments.
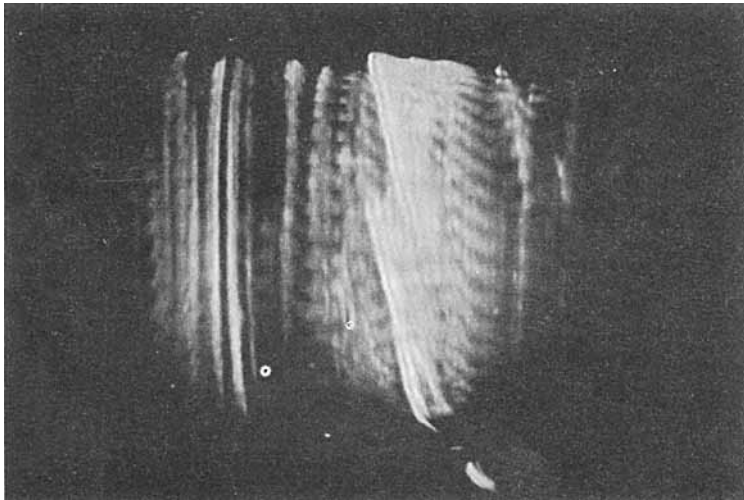

FIGURE 11. The motion around the cylinder at $K_c = 0.3$, showing the first indication of axial motion.

steady state, whereas the measurements were made after the loading had become periodic.

From velocity measurements made with a propeller meter, Otsuka *et al.* inferred the circulation around a horizontal cylinder beneath waves, at a radius of 1.15. Velocity components u_0 interpolated from their results at $K_c = 1.0$ and 1.5, shown in figure 6 (*a*), indicate a recirculating current of the same order as those computed here, but the data points otherwise offer little scope for comparison.

With the aim of investigating one of the differences between the experiments and numerical models, some simple flow visualization was carried out to reveal the existence of any three-dimensional structure in the flow around a horizontal cylinder beneath waves. The sketch in figure 10 shows the layout of the experiments in which solder was precipitated, by the method described by Honji (1981) and Sarpkaya (1986), to provide flow visualization. A 50 mm diameter cylinder spanned the 750 mm width of a wave flume, in which the mean water depth was 500 mm. The
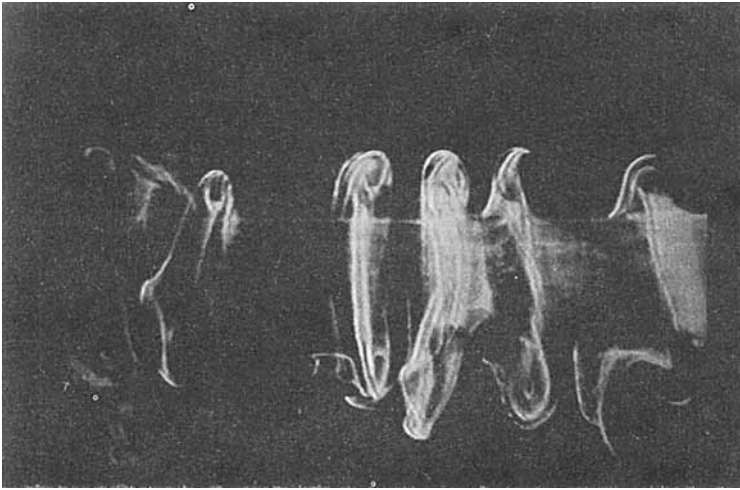
FIGURE 12. Toroidal vortices around the cylinder at $K_c = 0.65$.

cylinder was simply jammed between the glass sidewalls of the flume, at an elevation of 300 mm above the bed, thus avoiding the disturbance to the flow that would be created by other means of support. A thin solder wire was stretched along the side of the cylinder away from the wave generator, and energized at about 13 V. A beam of light parallel to the cylinder axis illuminated the flow, which was viewed from above, through the water surface.

As successive waves passed, the effect of steady streaming was to sweep the precipitate around the cylinder circumference. Figure 11 shows the flow at $K_c = 0.3$, with a wave period of 1 s. The striations in the precipitate parallel to the cylinder axis result from the oscillatory nature of the flow past the solder wire. In this case the flow was nearly two-dimensional, but there is evidence of some motion in the axial direction. At larger amplitudes this developed into a definite structure of toroidal vortices of alternating senses of rotation, as shown in figure 12 for $K_c = 0.65$.

The orbital motion in this experiment was neither uniform nor circular; the orbit elipticity was 0.85. The importance of the instability in other cases cannot yet be assessed, but it is likely to have a significant effect on the strength of the outer recirculating flow which, as shown above, is closely related to the nonlinear components of loading. It may be concluded that in at least some cases, numerical models which assume that the flow is two-dimensional cannot be expected to provide results that are in good agreement with measurements.

6. Conclusions

Numerical modelling of two-dimensional time-dependent circular orbital laminar flow around a circular cylinder has produced results that in most respects converge towards those of an analytical solution by Riley (1971), as β is increased. The outer recirculating flow however never reaches the steady state predicted by Riley, and related force components (namely the pressure force in anti-phase with the ambient acceleration, and the moment) likewise never reach stable values after any finite time. Indeed at all times the outer flow at high values of β is nearly identical to that generated by a cylinder rotating with surface speed $3K_c/\pi$ in fluid otherwise at rest.

At $\beta = 500$, Riley's solution remains reasonably accurate up to $K_c = 0.5$, at which the amplitude of the motion is about 8 % of the cylinder diameter. As K_c is increased further, the recirculating flow becomes disproportionately stronger, leading to an enhancement of the viscous loading, which at $K_c = 1.5$ (but before gross separation occurs) negates almost one-half of the potential flow force.

At K_c between 1.3 and 1.5, the retrogressive movement of vortex structures around the cylinder is responsible for a component of loading at a frequency of about 30 % of that of the ambient motion. This may be of concern in the context of compliant offshore structures.

Numerical results suggest a nonlinear force rather stronger than that observed in experiments. However, visualization experiments have revealed for the first time a three-dimensional structure that must in practice have an important effect on the outer flow, and therefore on the related nonlinear loading. The axial component of motion is absent in the numerical modelling, which has nevertheless served to develop an understanding of the flow, and which will provide a basis for future computations in three-dimensions.

Appendix. Velocity components derived from Riley (1971)

For the purposes of the present paper, Riley's results have been expressed in a different form. The tangential velocity components defined in (3.1) and (3.2) may be written as follows. In each case the highest orders of the truncated terms are indicated.

For the outer region:

$$u_0 = K_c[-(3/\pi r) + O(\beta^{-\frac{1}{2}})] + O(\beta^{-1}) + O(K_c^2), \tag{A 1}$$

$$u_1 = (2/r^2)(\pi\beta)^{-\frac{1}{2}} + O(\beta^{-1}) + O(K_c^2), \tag{A 2}$$

$$v_1 = -1 - (1/r^2) - (2/r^2)(\pi\beta)^{\frac{1}{2}} + O(\beta^{-1}) + O(K_c^2), \tag{A 3}$$

$$u_2 = O(\beta^{-1}) + O(K_c^2), \quad v_2 = O(\beta^{-1}) + O(K_c^2). \tag{A 4}, (A 5)$$

For the inner region, where the ordinate η is defined in (3.3):

$$U_0 = K_c\{[2(2\cos\eta - \sin\eta)\,\mathrm{e}^{-\eta} + 2(\cos\eta + \sin\eta)\,\eta\mathrm{e}^{-\eta} - \mathrm{e}^{-2\eta} - 3]/\pi$$
$$+ O(\beta^{-\frac{1}{2}})\} + O(\beta^{-1}) + O(K_c^2), \tag{A 6}$$

$$U_1 = -2\mathrm{e}^{-\eta}\sin\eta + 2[1 - (\cos\eta + \sin\eta)\,\mathrm{e}^{-\eta} + \eta\mathrm{e}^{-\eta}\sin\eta]\,(\pi\beta)^{\frac{1}{2}}$$
$$+ O(\beta^{-1}) + O(K_c^2), \tag{A 7}$$

$$V_1 = 2(\mathrm{e}^{-\eta}\cos\eta - 1) + 2[2\eta - 1 + (\cos\eta - \sin\eta)\,\mathrm{e}^{-\eta} - \eta\mathrm{e}^{-\eta}\cos\eta]\,(\pi\beta)^{-\frac{1}{2}}$$
$$+ O(\beta^{-1}) + O(K_c^2), \tag{A 8}$$

$$U_2 = K_c\{[\mathrm{e}^{-\eta}\cos\eta - (\cos\eta + \sin\eta)\,\eta\mathrm{e}^{-\eta} - \mathrm{e}^{-\sqrt{2}\eta}\cos\sqrt{2}\eta]\,2/\pi + O(\beta^{-\frac{1}{2}})\}$$
$$+ O(\beta^{-1}) + O(K_c^2), \tag{A 9}$$

$$V_2 = K_c\{[\mathrm{e}^{-\eta}\sin\eta + (\cos\eta - \sin\eta)\,\eta\mathrm{e}^{-\eta} - \mathrm{e}^{-\sqrt{2}\eta}\sin\sqrt{2}\eta]\,2/\pi + O(\beta^{-\frac{1}{2}})\}$$
$$+ O(\beta^{-1}) + O(K_c^2). \tag{A 10}$$

REFERENCES

BATCHELOR, G. K. 1967 *An Introduction to Fluid Dynamics.* Cambridge University Press.

CHAPLIN, J. R. 1984*a* Mass transport around a horizontal cylinder beneath waves. *J. Fluid Mech.* **140**, 175–187.

CHAPLIN, J. R. 1984*b* Forces on a horizontal cylinder beneath waves. *J. Fluid Mech.* **147**, 449–464.

CHAPLIN, J. R. 1992 Orbital flow around a circular cylinder. Part 1. Steady streaming in non-uniform conditions. *J. Fluid Mech.* **237**, 395–411.

CHAPLIN, J. R. & RETZLER, C. H. 1991 Non-linear pontoon loading. Report to the Department of Energy, TA 93/22/399.

EVANS, D. V. 1976 A theory for wave-power absorption by oscillating bodies. *J. Fluid Mech.* **77**, 1–25.

GOLDSTEIN, S. 1932 Some two-dimensional diffusion problems with circular symmetry. *Proc. Lond. Math. Soc.* (2) **34**, 51–88.

HONJI, H. 1981 Streaked flow around an oscillating circular cylinder. *J. Fluid Mech.* **107**, 509–520.

LONGUET-HIGGINS, M. S. 1970 Steady currents induced by oscillations round islands. *J. Fluid Mech.* **42**, 701–720.

OTSUKA, K., IKEDA, Y. & TANAKA, N. 1990 Viscous forces acting on a horizontal circular cylinder in regular and irregular waves. *Proc. 9th Intl Conf. on Offshore Mechanics and Arctic Engineering,* vol. 1, pp. 129–138.

PATEL, V. A. 1976 Time-dependent solutions of the viscous incompressible flow past a circular cylinder by the method of series truncation. *Computers Fluids* **4**, 13–27.

RILEY, N. 1971 Stirring of a viscous fluid. *Z. Angew. Math. Phys.* **22**, 645–653.

SARPKAYA, T. 1986 Force on a circular cylinder in viscous oscillatory flow at low Keulegan–Carpenter numbers. *J. Fluid Mech.* **165**, 61–71.

STANSBY, P. K. & SMITH, P. A. 1991 Viscous forces on a circular cylinder in orbital flow at low Keulegan–Carpenter numbers. *J. Fluid Mech.* **229**, 159–171.

WU, J. C. 1981 Aerodynamic force and moment in viscous flows. *AIAA J.* **19**, 432–441.